Investigation of the fusion mechanism in the ^{6}Li-induced reaction on ^{93}Nb

Ankur Singh👁 and Moumita Maiti👁*

Department of Physics, Indian Institute of Technology Roorkee, Roorkee 247667, Uttarakhand, India

We attempt to put forth the competing reaction mechanisms through residual cross section measurement in ^{6}Li fusion with ^{93}Nb. The measured residual cross sections in the 24–43 MeV energy range are analyzed with the theoretical estimations from PACE4, EMPIRE3.2.2, and ALICE23 statistical model codes. The replication of major xn-channel cross sections by EMPIRE with enhanced generalized superfluid model (EGSM) level density confirms that the population of xn-channel residues is through the complete fusion (CF) mechanism. The preequilibrium (PEQ) emission signatures were witnessed in the case of ^{97}Ru residue populated via the $2n$ channel. Amplification of major experimental p- and α-channel cross sections relative to the optimal theory was interpreted by considering the possibility of an incomplete fusion (ICF) process in addition to CF, owing to the low breakup threshold of the ^{6}Li projectile. Thus, the ICF strength fraction (F_{ICF}) was estimated. The F_{ICF} turned out to be ≈8–20% with an increasing trend and is found to be thoroughly higher than the deduced F_{ICF} for ^{7}Li reaction on ^{93}Nb target. In the case of weakly bound ^{6,7}Li-induced reactions, the first attempt is made to understand the influence of entrance channel parameters such as bombarding energy, α-separation energy, Coulomb factor, mass asymmetry, neutron skin thickness, angular momentum, etc., on F_{ICF}. The observed trend of the isomeric cross section ratios from the relative population of isomeric and ground states of ^{96,94}Tc radionuclides is also discussed.

I. INTRODUCTION

Advancements in accelerator technologies and measurement techniques are facilitated for probing microscopic nuclear properties and reaction dynamics. The energy and angular momentum imparted by a projectile in heavy-ion reactions disperse into the kinematically driven complex reaction dynamics involving multifold degrees of freedom. Besides the dominant complete fusion (CF), weakly bound particle induced reactions result in competing breakup fusion (ICF) and/or transfer mechanisms [1], subject to the energy domain of study. The breakup threshold anomaly of weakly bound particles has remained a hotly debated topic for more than a decade [2], as they embody a gateway to perceiving astrophysical nucleosynthesis. Nevertheless, inadequacy in the absolute understanding of mechanisms and ambiguous findings prevail in the literature, entailing extensive efforts from researchers, especially in the light-medium mass region where the competing mechanisms populate the same channel, in contrast to the heavy mass region where the strong Coulomb force restricts the emission of charged particles. The breakup of the projectile prior to fusion influences the fusion cross sections causing a loss of flux from the CF channel, thus, giving rise to fusion suppression at above-barrier energies relative to the one-dimensional barrier penetration model (1D-BPM) and/or coupled-channel (CC) calculations [3–6]. Successively, ≈15–30% [7,8] and ≈30–40% [3–6,9] of fusion suppression due to breakup have been estimated

in weakly bound induced reactions on medium and heavy mass targets, respectively. Furthermore, an increasing trend of suppression factor with target charge (Z_T) is suggested in Ref. [5], contrary to an independency reported by Kumawat *et al.* [7]. ^{6}Li prompt breakup into $\alpha + d$ arises from the breakup couplings in the continuum, although in-beam studies mark the resonant breakup as well [10,11]. Transfer-triggered breakup channels such as $\alpha + p$ and $\alpha + \alpha$ have also been argued in the literature [10–12]. The disentanglement of prompt breakup contribution from the transfer-triggered breakup poses an experimental limitation due to the population of the same resulting channels by the duo. However, the dominance of prompt/resonant $\alpha + d$ breakup of ^{6}Li over transfer-triggered breakup channels is discussed in Ref. [11], contrary to Ref. [12]. Moreover, at a particular beam energy, a linear rise of nuclear and Coulomb breakup components of ^{6}Li with $A_T^{1/3}$ and Z_T, respectively, was reported by Otomar *et al.* [13], where A_T and Z_T stand for the mass and charge of the target, respectively.

Inclusive of breakup fusion, preequilibrium (PEQ) emissions may emerge from the hot composite system [to attain a sustainable angular momentum for the formation of a compound nucleus (CN)] preceding the statistical equilibrium. PEQ has been predominantly observed in the n-emitting channels at high excitation energies relative to equilibrium (EQ) reaction-based statistical model calculations [14,15]. The early evidence of ICF dates back to an observation of high energy α-emission in the forward cone in ^{12}C, ^{14}N, and ^{16}O reactions on Au and Bi studied by Britt and Quinton [16]. Since then, persistent efforts have been put forth employing distinct measurement techniques to understand an obscure onset of

─────────
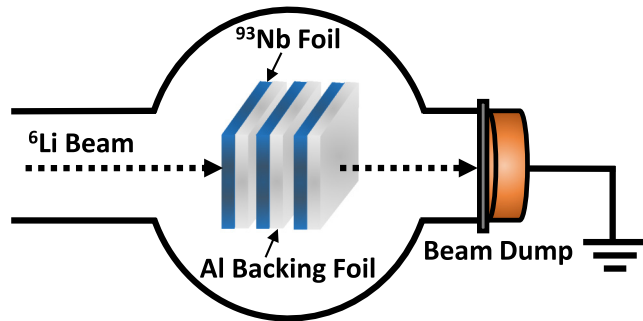*Corresponding author: moumita.maiti@ph.iitr.ac.in

FIG. 1. Prototype of typical target-catcher matrix adopted for the experiment.

ICF along with the production of neutron-deficient radioisotopes in low energy reactions using well bound α-clustered beams [17–24]. Subsequently, the influence of entrance channel parameters, such as projectile energy, α-separation energy, Coulomb factor ($Z_P Z_T$), target neutron skin thickness, mass asymmetry (μ), target deformation (β), and angular momentum, on ICF strength fraction (F_{ICF}) has been explored [17–22]. In this sequence, a linear rise of F_{ICF} with projectile energy, $Z_P Z_T$, and μ was suggested in Refs. [18,19], while an exponentially growing F_{ICF} trend with $Z_P Z_T$, μ, and β was concluded by Giri *et al.* [21]. However, a monotonic F_{ICF} trend with Z_T was reported in Ref. [22], contrary to an independency discussed in Ref. [25]. Moreover, recent studies [19,26] reflect the ICF onset below the critical limit of input angular momentum contrary to the sharp cutoff approximation [27]. An extensive literature survey shows scarce ICF data and no ICF systematics for weakly bound (^{6,7}Li, ^{9}Be) induced reactions over the entire mass domain. In this endeavor, for the first time, we present F_{ICF} systematics with entrance channel parameters to conclude the effect of ^{6,7}Li reactions on medium mass targets. However, the dearth of ICF data and cryptic findings reported in the literature require more ICF data generation encompassing the entire mass region to concretize the ICF onset and supplement the F_{ICF} trend observed in this paper.

We report a study of competing reaction mechanisms through measured residual cross sections in ^{6}Li fusion with ^{93}Nb within the 24–43 MeV energy range. The organization of this article is as follows: Experimental technique and theoretical framework are discussed in Secs. II and III, respectively. Section IV reports the experimental findings comprising excitation function analysis, CF-ICF analysis, F_{ICF} systematics, and isomeric cross section ratio. Section V summarizes the paper.

II. EXPERIMENTAL TECHNIQUE

Target preparation. The self-supporting rolled ^{93}Nb foils having thickness $\approx$1.3–2.2 mg/cm^2 were arranged in an alternating fashion (Fig. 1) to fabricate the target-catcher matrix with Al catchers of thickness $\approx$1.5–1.8 mg/cm^2 acting as backing to each target foil. A total of 11 Al-backed target foils divided into four sets of stack corresponding to four distinct sets of irradiation were utilized in the measurements.

Irradiation. ^{6}Li^{+3} ions of energy in the range 24.2–42.8 MeV delivered by the BARC-TIFR Pelletron facility, Mumbai, India, impinged upon the target matrices. Four sets of irradiation of varying energies, 43, 40, 33, and 28 MeV, on four different target-catcher stacks consisting of three, two, three, and three Al-backed Nb layers, respectively, were carried out. Two to three target-catcher layers in a stack were chosen to avoid energy straggling and allow the uninterrupted transmission of incident flux through the stack to measure irradiated dose or beam current at the Faraday cup. The average ion-beam flux and irradiated charge were $\approx$5.8 × 10^{10} particles/s and $\approx$206 μC, respectively. Unaltered beam current was preserved during the experiment, and the beam was dumped into the Faraday cup located downstream at the rear of the target matrix. Monte Carlo simulation based SRIM code [28] was employed to compute the energy degradation through each target and catcher foil. The requisite energy points were obtained by averaging the energies at the entrance and exit of the foils. Irradiation time was derived from the half-lives of the residues expected in the reaction.

Activity measurement. Activated target foils were assayed post-irradiation using a precalibrated high resolution ($\leqslant$2.0 keV at 1332 keV energy γ-ray of ^{60}Co) high-purity germanium (HPGe) detector coupled to a PC through the multichannel analyzer. A precise energy and efficiency calibration of the detector was performed using the standard sources ^{152}Eu (13.506 yr), ^{137}Cs (30.08 yr), and ^{60}Co (5.27 yr) of known strengths, prior to the measurements. The populated residues were identified from their characteristic γ lines in the recorded spectrum and experimental decay curves. The background subtracted and dead time ($<$10%) corrected photopeak statistic was utilized to estimate the production cross sections of residues employing the activation formula [29,30]

$$\sigma_i(E) = \frac{\lambda_i A_i^\gamma}{I_i^\gamma \varepsilon_i^\gamma \phi \rho_t z_t (e^{-\lambda_i t_w})(1 - e^{-\lambda_i t_r})(1 - e^{-\lambda_i t_c})}, \quad (1)$$

where λ_i is the decay constant of ith residue, A_i^γ is photopeak statistics, I_i^γ is the intensity of the characteristic γ line, ε_i^γ is the geometry dependent detection efficiency, ϕ is the incident beam flux, ρ_t is the nuclei per unit volume of the target foil, z_t is the target foil thickness, t_w is the cooling time, t_r is the irradiation time, and t_c is the counting time in the expression. Table I displays the nuclear spectroscopic data utilized in evaluating residual cross sections.

Sources of error. The reported experimental data are associated with an average uncertainty of $\approx$10–12%, contributed by distinct factors, such as (i) $\approx$2% from the target thickness, (ii) $\leqslant$2% from the detection efficiency, (iii) $\approx$5–7% from the beam current fluctuations, (iv) uncertainty in photopeak statistics (from Gaussian fit of the peaks by GENIE2K software) ranging $\approx$0.2–3% for the intense peaks, and (v) uncertainty in beam energy due to energy loss at successive target-catcher foils and SRIM calculation.

III. THEORETICAL FRAMEWORK

The measured data were compared with theoretical estimations from statistical model codes PACE4 [32], EMPIRE3.2.2

TABLE I. Nuclear spectroscopic data [31] of residues populated in the ^{6}Li + ^{93}Nb reaction. The last column of the table denotes the reaction channel(s) through the CF mechanism with the reaction threshold in parenthesis.

Nuclide	J^π	$T_{1/2}$	Decay mode (%)	E_γ (keV) [I_γ (%)]	CF reaction channel (E_{th} [MeV])
^{97}Ru	$5/2^+$	2.83 d	ϵ[a] (100)	215.7 [85.62], 324.49 [10.79]	$2n$ (3.3)
^{95}Ru	$5/2^+$	1.643 h	ϵ (100)	290.38 [3.68], 301.01 [2.1]	$4n$ (23.2)
				336.4 [69.9], 626.83 [17.8]	
				806.28 [4.04], 1050.68 [2.6]	
				1096.8 [20.9], 1178.7 [5.13]	
				1410.63 [2.48], 1459.32 [2.09]	
^{94}Ru	0^+	51.8 min	ϵ (100)	367.2 [75]	$5n$ (32.7)
^{96}Tc	7^+	4.28 d	ϵ (100)	778.22 [99.76], 812.54 [82]	$p2n/t$ (11.3/2.3)
				849.86 [98], 1126.85 [15.2]	
^{96m}Tc	4^+	51.5 min	IT[b] (98), ϵ (2)	1200.15 [1.1]	$p2n/t$ (11.3/2.3)
^{95}Tc	$9/2^+$	20 h	ϵ (100)	765.789 [93.8], 947.67 [1.951]	$p3n/tn$ (19.7/10.7)
				1073.71 [3.74]	
^{94}Tc	7^+	293 min	ϵ (100)	449.2 [3.3], 702.67 [99.6]	$p4n/t2n$ (30.2/21.2)
				742.3 [1.21], 871.05 [99.9]	
				916.1 [7.6]	
^{94m}Tc	2^+	52 min	ϵ (100), IT (<0.1)	1522.1 [4.5], 1868.68 [5.7]	$p4n/t2n$ (30.2/21.2)
^{93m}Mo	$21/2^+$	6.85 h	IT (99.88), ϵ (0.12)	263.049 [57.4], 684.693 [99.9]	$\alpha2n$ (5.1)
				1477.138 [99.1]	
^{92m}Nb	2^+	10.15 d	ϵ (100)	934.44 [99.15]	$\alpha p2n/\alpha t$ (13.2/4.3)

[a]Electron capture.

[b]Isomeric transition.

[33], and ALICE23 [34] to comprehend the dynamics prevalent in reaction. Salient features of the codes with chosen sets of input parameters are discussed below.

PACE4. The code employs the Hauser-Feshbach (HF) formalism [35] to simulate the decay sequence of an excited CN formed through statistical equilibration of the composite system. A Monte Carlo approach with a large number of deexcitation cascades (100000 assumed here) correlates the γ deexcitations and angular distribution of emitted particles. An appropriate angular momentum coupling procedure is exploited at each CN deexcitation stage. The entrance-channel fusion cross section and spin distribution are estimated by the Bass model with quantum mechanical transmission probability ensured by the Hill-Wheeler's approach (using the default barrier curvature parameter). Sierk's modified rotating liquid drop fission barrier method treats the fission as a competing CN decay mode. Transmission coefficients for particle evaporation are estimated by the optical model (OM) importing parameters from the global systematics [36]. At higher excitation energies where the levels are closely spaced, level density is taken into consideration through the Gilbert-Cameron (GC) model (GC spin cutoff parameter is used) with variable level density parameter $a = A/K$, where A is the mass number of the CN, and K is free parameter varied to test the sensitivity of theoretical cross sections. Here, $K = 8$ is taken, although the sensitivity with $K = 9, 10$ was also tested while analyzing the data. The ARATIO and Yrast parameters are assumed to be unity in the present case. It should be noted that PACE works in the framework of CF dynamics only; thus, PEQ and direct (DIR) mechanisms remain unaccounted for here. It does not estimate the isomeric yields explicitly.

EMPIRE3.2.2. It is a statistical modular code that accounts for EQ, PEQ, and DIR mechanisms. HF model with width fluctuation correction (proposed by Hofmann, Richert, Tepel, and Weidenmüller) for EQ, phenomenological exciton model (EM) (with Iwamoto-Harada cluster emission and Kalbach systematic for angular distribution), and hybrid Monte Carlo simulation (HMS) for PEQ processes are adopted. A coupled-channel approach and distorted wave Born approximation (DWBA) estimate the DIR contribution. Simplified coupled-channel code CCFUS internally calculates the entrance-channel fusion cross section assuming independent consideration of the inelastic excitations and transfer channels that couple to the initial ground state. A complete γ cascade after particle emission with realistic treatment of discrete transitions is considered. OM evaluates the transmission coefficients for particle emission based on the systematics from Koning and Delaroche [37] for n and p, Haixia [38] for d, Becchetti and Greenlees [39] for t, and Avrigeanu [40] for α emission. Code imports the OM parameters, nuclear masses, level density, discrete levels, fission barriers, and γ strength functions from a built-in RIPL-3 library [41]. We have used the HF model with a model-default width fluctuation correction parameter for the EQ process and the EM model with 1.5 as the mean free path parameter controlled by the PCROSS module for the PEQ process. Three phenomenological level density models viz. Enhanced Generalized Superfluid Model (EGSM) [42], Generalized Superfluid Model (GSM) [43], and GC Model [44] are used here to reproduce the measured data. These level density models consider the effect of collective excitations on level density and exploit the energy-dependent Ignatyuk level density parameter, which considers the shell-effect-reliant

excitation energy. EMPIRE predicts the isomeric and ground state population separately.

ALICE23. The code, developed by Blann [34], incorporates the EQ and PEQ as fundamental decay mechanisms. It exploits the Weisskopf-Ewing (WE) model [45] for the EQ process, a Monte Carlo based hybrid (HMS) or a geometry-dependent hybrid model [34] to simulate the PEQ emission, and the Bohr-Wheeler method for the fission decay mode. The angular momentum conservation based model of Chadwick and Oblozinsky treats the angular distribution of ejectiles. The inverse cross sections for the residuals after particle emission are governed by the OM potential. During the evaporation process, the Q values and binding energies are evaluated by the Myers-Swiatecki-Lysekil mass formula with shell corrections. Ease of use is facilitated by several libraries, internal data files, and subroutines to prepare data necessary for the calculations. In the present analysis, we opted for WE and HMS (with 200000 cascade events) models for EQ and PEQ mechanisms, respectively. The availability of input options invoked at user discretion makes the code versatile. A rotational energy correction approximation (using parameter PARM = 20) is utilized to match the peaks of the experimental excitation functions. There is a provision to select different level density models like the Fermi gas (FG) model, Kataria-Ramamurthy (KR) model, GC model, and Obninsk model to get the best description of the experimental data. The FG model (back-shifted pairing energy) with level density parameter $K = 10$ and the KR model were used. It should be noted that KR and GC model calculations are invariant of K. We used the exciton distribution formula for the initial doorway configuration through the ICOUPLE = 0 parameter. However, one may opt for the default or user-defined actual random coupling with Fermi energy. ALICE calculates the isomeric yields independently.

IV. RESULTS AND DISCUSSION

A typical γ-spectrum recorded 46 min post bombardment from 43 MeV ^{6}Li irradiated ^{93}Nb foil is shown in Fig. 2. The acquired γ-spectrum analysis affirmed the production of ^{97,95,94}Ru, ^{96,96m,95,94,94m}Tc, ^{93m}Mo, and ^{92m}Nb residues in
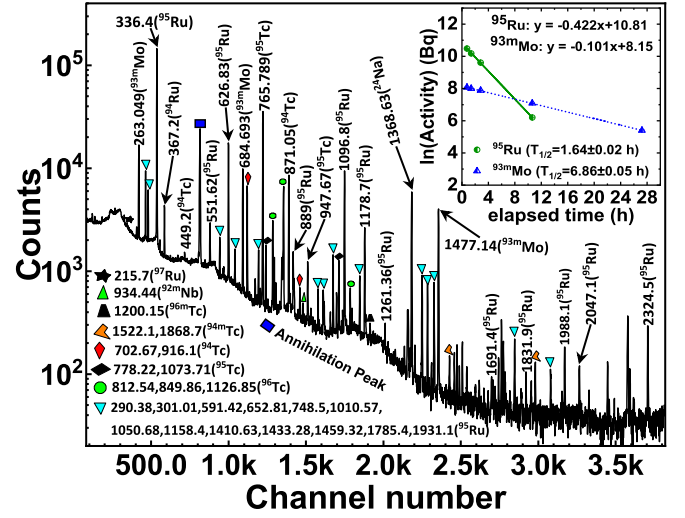
FIG. 2. Typical γ-ray spectrum acquired using GENIE2K software from ^{6}Li irradiated ^{93}Nb foil at 43 MeV bombarding energy. The γ peaks of residues are marked with energies in keV. The inset displays the experimental decay curves and deduced half-lives of ^{95}Ru and ^{93m}Mo residues. The experimental half-lives are close to the database values reported in Table I.

^{6}Li fusion with ^{93}Nb target in the studied energy range. The residues were identified from their characteristic γ lines and half-lives. Subsequently measured residual production cross sections are tabulated in Table II. Figures 3–5(a) outline the channelwise comparison of measured excitation functions of residues with the theoretical predictions from PACE4, EM-PIRE3.2.2, and ALICE23 model codes. Theoretical estimations are presented using curves, while the symbols represent the experimental data. ICF systematics for ^{6,7}Li-induced reactions on different target sets is discussed in Sec. IV C. Isomeric cross section ratios for the ^{96m,96}Tc and ^{94m,94}Tc isomeric pairs are also discussed in Sec. IV D.

TABLE II. Experimental cross sections of residues populated in the ^{6}Li + ^{93}Nb reaction at various incident energies.

| E_{Lab} (MeV)	Cross section (mb)									
	^{97}Ru	^{95}Ru	^{94}Ru	^{96}Tc	^{96m}Tc	^{95}Tc	^{94}Tc	^{94m}Tc	^{93m}Mo	^{92m}Nb
24.2 ± 0.6	56.9 ± 6.3			92.1 ± 10.4	57.4 ± 7.8	3.5 ± 0.5			4.4 ± 0.5	2.2 ± 0.6
25.8 ± 0.7	47.4 ± 5.4	0.1 ± 0.02		135.9 ± 14.4	76.7 ± 9.2	7.7 ± 0.9			9.4 ± 1.1	2.6 ± 0.7
27.5 ± 0.8	34.7 ± 4.1	1.8 ± 0.2		175.5 ± 18.2	84.8 ± 10.0	18.9 ± 2.4			15.4 ± 1.7	2.9 ± 0.9
29.3 ± 0.8	26.4 ± 3.3	9.3 ± 0.9		192.6 ± 20.9	86.8 ± 11.5	46.8 ± 6.3	0.1 ± 0.03		21.7 ± 2.5	3.9 ± 1.0
30.9 ± 0.8	19.9 ± 2.7	34.9 ± 3.4		236.1 ± 25.6	94.5 ± 11.1	106.0 ± 11.9	0.4 ± 0.07		33.4 ± 3.7	4.5 ± 1.2
32.6 ± 0.8	14.9 ± 2.3	77.3 ± 7.4		247.4 ± 24.9	84.8 ± 11.1	197.7 ± 21.8	1.0 ± 0.1		44.1 ± 4.8	5.0 ± 1.3
38.5 ± 0.9	5.4 ± 1.1	192.2 ± 19.2	0.2 ± 0.07	155.2 ± 16.8	51.3 ± 9.4	499.2 ± 53.7	6.9 ± 0.8	3.5 ± 1.0	55.4 ± 5.7	6.9 ± 1.6
39.7 ± 0.8	4.8 ± 1.0	201.7 ± 19.3	0.5 ± 0.1	124.9 ± 13.9	38.2 ± 9.2	568.8 ± 66.4	10.7 ± 1.2	4.8 ± 1.3	50.7 ± 5.3	7.5 ± 1.9
40.8 ± 0.9	4.1 ± 0.9	214.9 ± 20.5	1.2 ± 0.2	119.1 ± 13.7	29.9 ± 8.6	625.9 ± 71.5	16.0 ± 1.7	5.4 ± 1.4	54.1 ± 5.7	8.0 ± 2.2
41.8 ± 0.9	3.8 ± 1.0	249.8 ± 23.9	2.9 ± 0.4	113.5 ± 13.7	26.2 ± 7.8	681.4 ± 75.5	26.3 ± 2.7	9.4 ± 2.0	59.5 ± 6.1	9.1 ± 3.3
42.8 ± 0.9	3.2 ± 0.8	212.2 ± 20.3	4.6 ± 0.5	89.0 ± 10.7	25.1 ± 6.8	634.6 ± 70.9	30.9 ± 3.3	11.0 ± 2.1	49.1 ± 5.2	8.9 ± 2.1
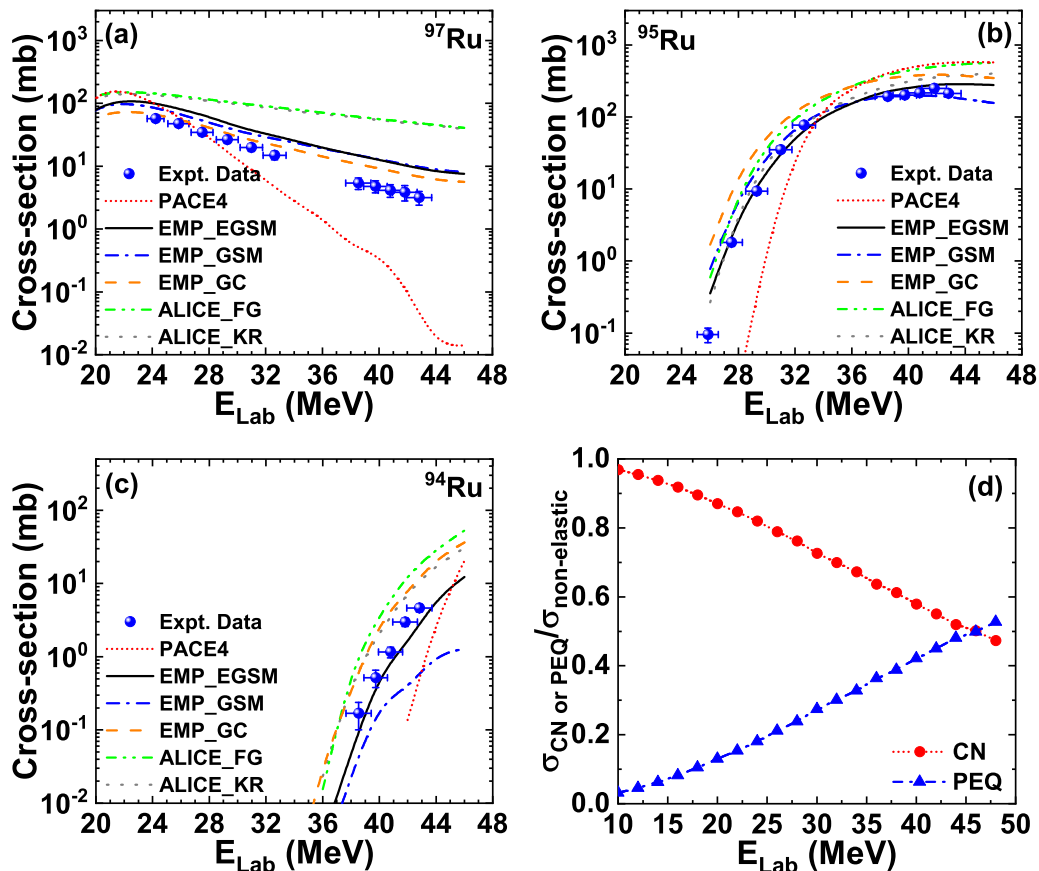
FIG. 3. The experimental excitation functions (solid blue symbols) of ^{97}Ru, ^{95}Ru, and ^{94}Ru residues populated via $2n$, $4n$, and $5n$ channels, respectively, compared with theoretical estimations from PACE4 with $K = 8$ (short dotted red curve), EMPIRE3.2.2 with EGSM (solid black curve), GSM (dash-dotted blue curve), and GC (dashed orange curve), and ALICE23 with FG (dash–double-dotted green curve) and KR (dotted grey curve) level densities. Panel (d) displays the relative contribution of CN (EQ) and PEQ processes in the reaction, predicted by EMPIRE code.

A. Excitation function analysis

xn channel. Neutron evaporation from the excited ^{99}Ru*
CN formed in the ^{6}Li + ^{93}Nb reaction yields the population of
^{97,95,94}Ru residues via $2n$, $4n$, $5n$ deexcitaton channels, respectively. Figure 3(a) displays the measured excitation function of
^{97}Ru in comparison with theoretical predictions such that the
PACE4 calculation explains the data in lower energy region up
to 29.3 MeV with a significant underestimation beyond it. Although superior to PACE4 estimates, EMPIRE predictions stand
close to the data in trend but with EGSM and GSM level densities (having almost overlapped yields) slightly surpassing
the data, while GC results complying with the data up to 30.9
MeV with an overestimation at higher energies. ALICE FG and
KR level densities predict similar cross sections far off the
data and exhibit a progressive deviation from EMPIRE yields.
The underestimation of data by PACE4 in the high energy tail
of the excitation function may be due to the PEQ emissions
at higher excitation energies that go uncounted in PACE4.
Thus, the data lie close to EMPIRE estimates, which consider
EQ+PEQ as fundamental decay mechanisms. A similar interpretation was given for ^{97}Ru populated via $3n$ channel in
^{7}Li + ^{93}Nb reaction [15]. Figure 3(b) shows the experimental
excitation function of ^{95}Ru residue thoroughly reproduced by

EMPIRE EGSM and GSM calculations, whereas GC traces out
higher cross sections in trend. PACE4 exhibits dramatic behavior of underestimation below 32.6 MeV and overestimation
above it. ALICE FG results in a gradual deviation from the data
over the entire energy range, while the KR calculation remains
in line with data up to 32.6 MeV with slightly augmented
yields above this energy point. EMPIRE EGSM fairly matches
the measured data of ^{94}Ru reported in Fig. 3(c). EMPIRE GC
overvalues the data same as ALICE FG and KR, while GSM
acting conversely. However, EMPIRE GC and ALICE KR predict
similar cross sections, while PACE4 estimates lie far below the
data. It should be stressed that a significantly low population
of the ^{94}Ru ($5n$ channel) compared to other n channels can be
speculated, as the $5n$ emission is quite unlikely to happen at
CN excitation energy $E^* \approx 37.3$–54.7 MeV (at incident energies). Sequential $5n$ emission from ^{99}Ru* CN exhausts ≈ 45.3
MeV energy. Thus, it leads to a substantially low population
of the $5n$ channel with available energy, which ceases below
38.5 MeV energy. Excitation function analysis for n-channel
residues indicates a better data reproduction by EMPIRE code
over the other two; thus, the population of Ru isotopes via the
CF mode followed by the equilibration of CN. The role of
EQ+PEQ mechanisms has been witnessed in the case of ^{97}Ru
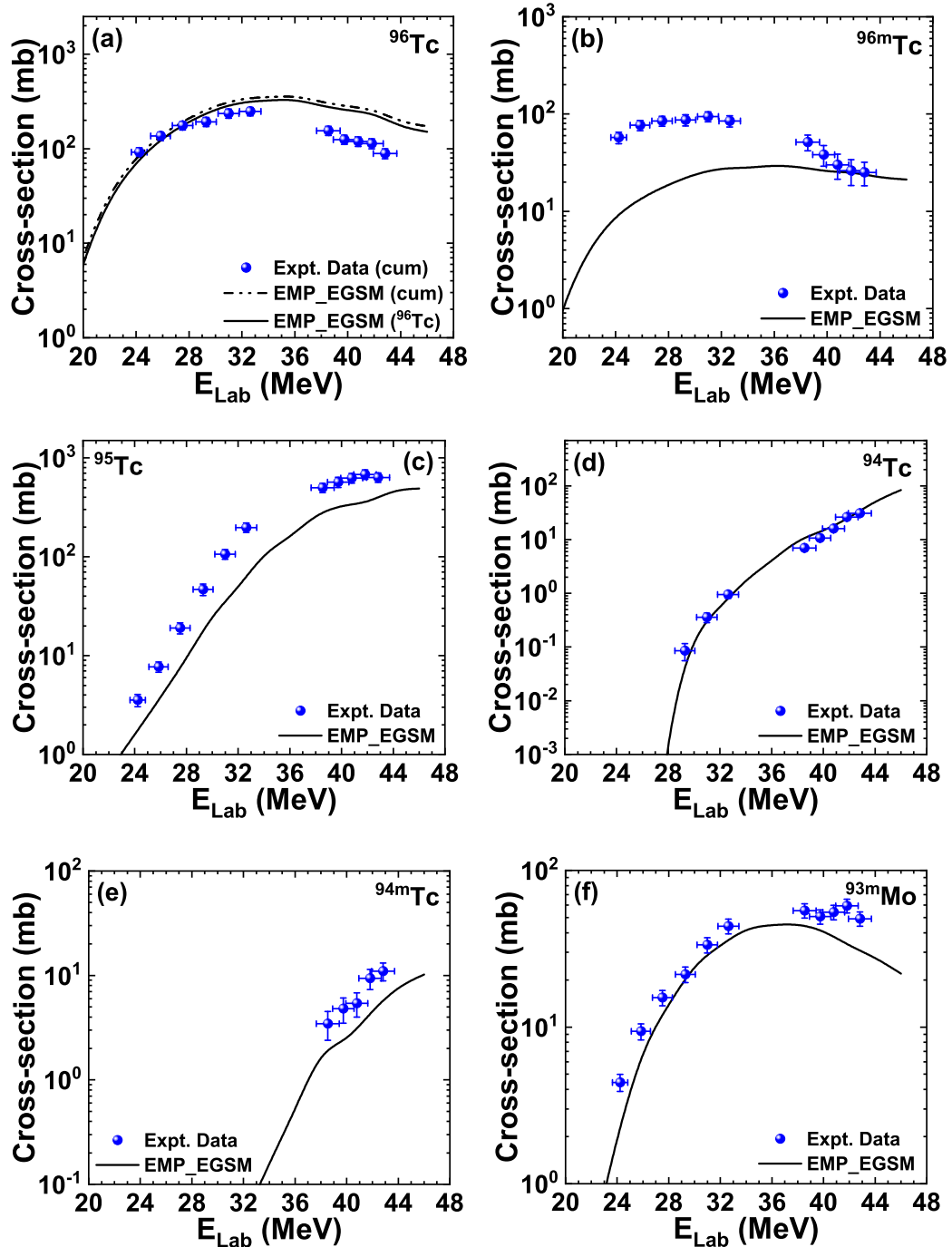residue. Moreover, the relative contribution of CN (EQ) and

FIG. 4. The experimental excitation functions of ^{96,96m}Tc, ^{95}Tc, ^{94,94m}Tc, and ^{93m}Mo residues populated via $p2n$, $p3n$, $p4n$, and $\alpha 2n$ channels, respectively, compared with optimal EMPIRE EGSM predictions. The dash–double-dotted curve in (a) denotes the theoretical cumulative yields for ^{96}Tc.

PEQ processes in the ^{6}Li + ^{93}Nb reaction could be assessed from the EMPIRE predicted total capture (nonelastic), CN, and PEQ cross sections [46] within the studied energy domain. From Fig. 3(d), one can notice that the EQ contribution dominates at lower energies and exhibits a dying-out character with rising energies, while PEQ significantly competes with EQ at higher excitation energies and dominates beyond ≈ 46 MeV for the present case. Quantitatively, for instance, at

24 MeV the total EQ and PEQ contributions from EMPIRE predictions are $\approx 82\%$ and 18%, respectively, while at 44 MeV the values stand close to $\approx 52\%$ and 48%, respectively. This indicates the increasing PEQ contribution with an increase in projectile energy. Amongst three level densities of EMPIRE code, EGSM shows exceptional predictive capability for major n-channel cross sections as reflected in previous studies [15,26]; hence, it has been chosen as the optimum
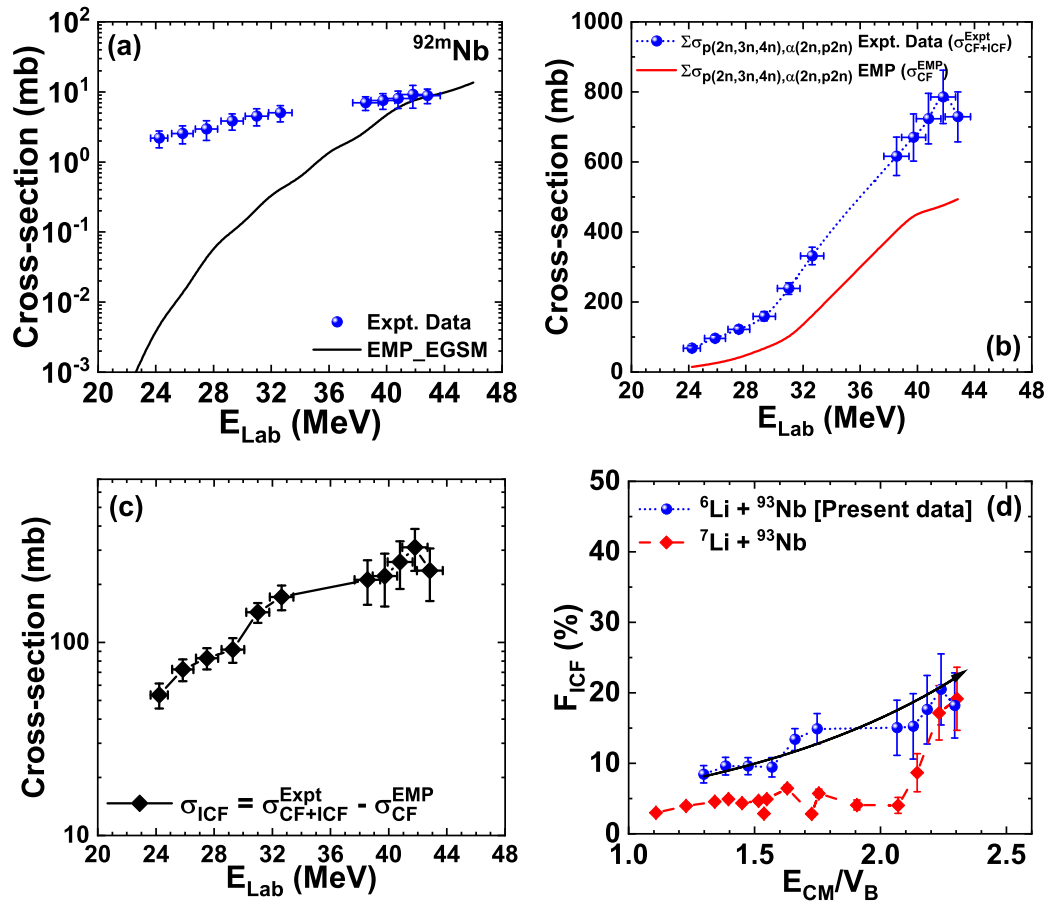
FIG. 5. (a) Same as Fig. 4 but for ^{92m}Nb residue populated via the $\alpha p2n$ channel. (b) Comparison of the measured cross sections (σ_{CF+ICF}) with theoretical cross sections (σ_{CF}) from EMPIRE EGSM for the ICF depicting channels. Panel (c) showcases the deduced ICF cross sections as a function of projectile energy. (d) Variation of ICF strength fraction (F_{ICF}) with normalized projectile energy for ^{6,7}Li + ^{93}Nb systems. The line joining the data is to guide the eyes. Refer to the text for details.

level density for subsequent analysis with the same set of input parameters.

pxn channel. Proton-plus-neutron deexcitation channels from CN populate the Tc residues. Accompanying the ground states of ^{96,94}Tc residues, isomeric states have also been populated significantly. Figure 4(a) portrays the measured cross sections of ^{96}Tc in comparison with EMPIRE EGSM estimates, which describe the data in a lower energy bracket up to 32.6 MeV, and a significant overprediction is seen above this energy. It is noteworthy that ^{96}Tc could be populated via two modes i.e., the ^{93}Nb(^{6}Li, $p2n$) ^{96}Tc reaction or the decay of short-lived metastable state ^{96m}Tc, ^{93}Nb(^{6}Li, $p2n$) ^{96m}Tc $\longrightarrow$ ^{96}Tc, may feed it through IT (98%). The measured data may have a contribution from both the modes, thus they are compared with the cumulative EMPIRE EGSM cross sections (dash-double-dotted curve) in Fig. 4(a) as suggested in Ref. [26]. The theoretical ^{96}Tc and ^{96}Tc (cumulative) cross sections differ by a factor of ≈ 0.09. No possible reason could be anticipated for the suppression of experimental cross sections compared to theory at higher energies. However, a similar excitation function trend was also observed for the $p2n$ channel in the ^{6}Li + ^{89}Y reaction [26]. There is a significant

enhancement in ^{96}Tc isomeric state cross sections throughout the energy domain relative to EMPIRE EGSM calculations, as shown in Fig. 4(b), except for two higher energy points where data overlap the theory. The experimental excitation function of ^{95}Tc residue populated via $p3n$ channel exhibits substantially enhanced values in trend compared to the reference theoretical values, as depicted in Fig. 4(c). The measured data of ^{95}Tc produced via $p4n$ channel in the ^{7}Li + ^{93}Nb reaction reported by Kumar *et al.* [15] also depict enhancement relative to optimum EMPIRE EGSM yields. The measured cross sections of ^{94}Tc thoroughly imitate the optimal theoretical cross sections reported in Fig. 4(d), while the measured isomeric state cross sections of ^{94}Tc demonstrated in Fig. 4(e) show the enhancement relative to theory. It is worth mentioning that the population of ^{94m}Tc appears in a higher energy window of 38.5–42.8 MeV due to energetically ceasing production in the lower energy side as the ground state population takes over at the lower excitation energies.

α(xn, pxn) channel. From the α-emitting channels we could identify ^{93m}Mo residue which was populated via the $\alpha 2n$ CN deexcitation channel. The measured data of ^{93m}Mo [Fig. 4(f)] apparently show the inferior degree of enhancement
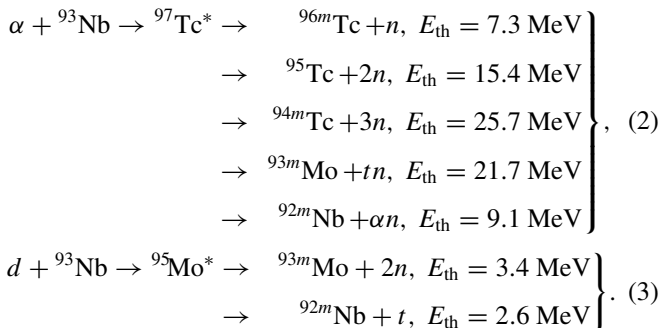
(minor) relative to optimum theoretical calculations at lower energies up to 32.6 MeV, while a considerable enhancement can be seen at higher energies. α emission along with a proton and two neutrons from the CN yield ^{92m}Nb residue having thoroughly higher cross sections compared to optimal level density predictions over the studied energy range [Fig. 5(a)], except for two higher energy points coinciding with theory. The measured low cross sections for the $\alpha p 2n$ channel can be ascribed to similar kinematical reasons as for ^{94}Ru.

The facts from p- and α-channel analysis assert the role of the CF mechanism in the production of ^{96,94}Tc residues. The significant enhancement observed in the case of ^{96m,95,94m}Tc, ^{93m}Mo, and ^{92m}Nb residues can be interpreted as being due to the alleged role of the ICF mechanism in addition to the dominant CF, attributed to the low breakup threshold of the weakly bound projectile (^{6}Li) [26,30,47–49]. The following subsection discusses the relevant CF-ICF analysis on account of the observed enhancement in major p- and α-channel cross sections.

B. CF-ICF analysis

A comprehensive excitation function analysis indicates the dominance of the CF mechanism for populating n- and a few p-channel residues, while the coaction of CF-ICF modes has been assumed in the population of ^{96m,95,94m}Tc, ^{93m}Mo, and ^{92m}Nb residues. In the CF mechanism, the ^{6}Li projectile entirely fuses while interacting with the ^{93}Nb target. The production feasibility of all the identified residues from ^{99}Ru* CN (formed with $E^* \approx 37.3$–54.7 MeV at incident energies) via different deexcitation channels may be inferred from the reaction thresholds (Table I) being lower than E^* of CN, favoring the population of channels. The possibility of t emission has also been considered in accordance with assumptions in theoretical models.

In an alternative competing fusion mechanism (ICF), owing to the weakly bound nature of the projectile used, ^{6}Li gets dissociated into two fragments ($\alpha + d$) in the field of the target nucleus. This results in reduced CN ^{97}Tc*(^{95}Mo*) emerging from the fusion of either of the fragments α (d) with ^{93}Nb, and complementary fragment d (α) moving unfused as spectator in the beam direction. Evaporation of light particles followed by γ emission from the reduced CN yields the residues; one can readily understand the formation of these residues via the ICF mechanism in terms of reaction thresholds as follows:

$$\alpha + {}^{93}\text{Nb} \rightarrow {}^{97}\text{Tc}^* \rightarrow \left.\begin{array}{l} {}^{96m}\text{Tc} + n, \ E_{\text{th}} = 7.3 \text{ MeV} \\ {}^{95}\text{Tc} + 2n, \ E_{\text{th}} = 15.4 \text{ MeV} \\ {}^{94m}\text{Tc} + 3n, \ E_{\text{th}} = 25.7 \text{ MeV} \\ {}^{93m}\text{Mo} + tn, \ E_{\text{th}} = 21.7 \text{ MeV} \\ {}^{92m}\text{Nb} + \alpha n, \ E_{\text{th}} = 9.1 \text{ MeV} \end{array}\right\}, \ (2)$$

$$d + {}^{93}\text{Nb} \rightarrow {}^{95}\text{Mo}^* \rightarrow \left.\begin{array}{l} {}^{93m}\text{Mo} + 2n, \ E_{\text{th}} = 3.4 \text{ MeV} \\ {}^{92m}\text{Nb} + t, \ E_{\text{th}} = 2.6 \text{ MeV} \end{array}\right\}. \ (3)$$

Equations (2) and (3) point out the production channels of residues via α-ICF and d-ICF, respectively, along with their

respective reaction thresholds. Reaction energetics favor the breakup fusion dynamics because, in the α-ICF (or d-ICF) mode, the fragment's energy [29] $E_\alpha = 15.2$–27.6 MeV (or $E_d = 7.6$–13.8 MeV for projectile incident energies) yields the reduced CN ^{97}Tc* (or ^{95}Mo*) at $E^* \approx 17$–28.9 MeV (or $E^* \approx 21$–27.1 MeV). The reaction thresholds, being lower than (or in the range of) the respective E^*, refer to the feasible yield in ICF channels. Therefore, the estimation of high experimental yields for ^{96m,95,94m}Tc, ^{93m}Mo, and ^{92m}Nb residues relative to theory has been observed. Moreover, Tc residues will be populated merely via α-ICF, whereas Mo and Nb residues have contributions from both α- as well as d-ICF modes. However, d capture by ^{93}Nb dominates over α capture as inferred from the lesser reaction thresholds for d capture than α capture and suggested in studies [26,50]. Besides the prompt/resonant breakup process, there could be a role of transfer-triggered breakup processes in the residual population, as reported in Refs. [10–12]. In this series, Owing to the positive Q value (+1.6 MeV), the feasible $1n$-stripping process (^{6}Li + ^{93}Nb $\rightarrow$ ^{94}Nb + ^{5}Li) and subsequent breakup of ^{5}Li into $\alpha + p$ might result in the production of ICF manifesting residues through α (or p) fusion with ^{93}Nb or ^{94}Nb target nuclei. The d-pickup process (^{6}Li + ^{93}Nb $\rightarrow$ ^{91}Zr + ^{8}Be) followed by the prompt/resonant dissociation of ^{8}Be into $\alpha + \alpha$ in the target field may also be possible because the positive ground state Q value (+9.8 MeV) of the process is close to the optimum Q value in the studied energy range. Fusing either of these α's with ^{93}Nb or ^{91}Zr may also populate the ICF channels. However, the prompt/resonant $\alpha + d$ breakup channel may dominate the transfer-triggered $\alpha + p$ or $\alpha + \alpha$ breakup channels [11]. At the same time, explicit disentanglement of prompt and transfer-triggered breakup processes poses experimental challenges.

For a better insight into the reaction mechanisms in the present study, we have quantified the ICF contribution from the ICF-interpreted channels employing the data reduction method [26,47]. Total ICF cross sections were deduced at each incident energy using the expression, $\Sigma\sigma_{\text{ICF}} = \Sigma\sigma_{\text{CF+ICF}} - \Sigma\sigma_{\text{CF}}$, where $\Sigma\sigma_{\text{CF+ICF}}$ and $\Sigma\sigma_{\text{CF}}$ denote the sum of measured and the sum of EMPIRE predicted cross sections, respectively, for ^{96m,95,94m}Tc, ^{93m}Mo, and ^{92m}Nb channels as reported in Fig. 5(b). From Fig. 5(b), one can notice that the relative separation of the measured and theoretical cross sections increases with the rise in incident projectile energy, implying a surge in ^{6}Li breakup probability with bombarding energy as pointed in Ref. [26]. The effect can be seen in the increasing trend exhibited by the ICF cross sections reported in Fig. 5(c). Relative ICF degree in the reaction was estimated in terms of ICF strength fraction (F_{ICF}), defined as $F_{\text{ICF}} = \Sigma\sigma_{\text{ICF}}/\Sigma\sigma_{\text{TF}}^{th}$, where $\Sigma\sigma_{\text{ICF}}$ and $\Sigma\sigma_{\text{TF}}^{th}$ stand for the deduced total ICF cross sections and theoretical total fusion cross sections in the reaction, respectively. The computed F_{ICF} values reported in Fig. 5(d) also obey an increasing trend with projectile energy as exhibited by ICF cross sections and range ≈ 8–20% (or ≈ 1.6–4.1% per channel) over the studied energy domain. To emphasize the projectile structure effect on F_{ICF}, we also deduced the F_{ICF} values for the ^{7}Li + ^{93}Nb system [15,48] from the p and α channels interpreted as ICF channels by author(s) in reference to optimum EMPIRE EGSM level density

predictions. Although the individual channelwise ICF contribution has been reported in Ref. [48], we estimated the total ICF contribution in the ^{7}Li + ^{93}Nb reaction to compare with the present measurement. A comparison of F_{ICF} for ^{6,7}Li + ^{93}Nb reactions as a function of normalized energy is shown in Fig. 5(d). As expected, evidently more F_{ICF} has been estimated for the ^{6}Li induced reaction over the ^{7}Li reaction in the entire energy range, except for one extreme energy point dipped in the ^{6}Li case (in trend with ICF cross sections) which does not distort the conclusion. A similar F_{ICF} trend for the ^{6}Li reaction is also reported in Ref. [26]. The larger F_{ICF} values for the ^{6}Li reaction over ^{7}Li can be accredited to the higher breakup probability of ^{6}Li over ^{7}Li owing to even lesser breakup threshold $S_\alpha = 1.47$ MeV for ^{6}Li than $S_\alpha = 2.47$ MeV for ^{7}Li. Moreover, Morgenstern *et al.* [51] proposed the ICF onset at relative velocity $V_{rel} \geqslant 0.06c$ (i.e., 6% of the speed of light); given by $V_{rel} = \sqrt{2(E_{CM} - V_B)/\mu_m}$, where E_{CM}, V_B, and μ_m denote the projectile energy in the center of mass frame, Coulomb barrier, and reduced mass of the system, respectively. However, recent studies [18,20] including present measurements articulate the significant population of ICF channels at $V_{rel} < 0.06c$, contrary to what is indicated in Ref. [51]. Also, a sizable CF suppression (≈ 25–34%) above the barrier due to the breakup of ^{6}Li realized in nearby systems [7,8] corroborates the existence of ICF in the present study; however, the reported F_{ICF} may be recognized as the lower limit attributed to the missing channels unaccounted for in the adopted technique of measurement. So far, no theoretical model could fairly simulate the ICF dynamics within 3–7 MeV/A energies. Therefore, the generated ICF data would certainly enrich further theoretical refinements. A model (if developed in the future) which universally fits the ICF data over the entire mass domain can be integrated with the framework of EMPIRE code, allowing it to assess the several other processes appearing in the reaction dynamics, including EQ, PEQ, and DIR.

C. Entrance channel influence on F_{ICF}

This subsection reports the F_{ICF} systematics for ^{6,7}Li-induced reactions on different targets to portray the influence of several entrance channel parameters on ICF contribution as discussed below.

Projectile structure. As quoted in the previous subsection, projectile structure plays a vital role in the breakup fusion mechanism. Owing to the weakly bound nature and/or α-clustered structure of the projectile, larger ICF is expected for a projectile having a lesser magnitude of α-separation energy (S_α) among others when impinged upon the same target [19,26]. Figure 6(a) compares the F_{ICF} values for ^{6}Li (present data), ^{7}Li [48], and ^{12}C [17] induced reactions on ^{93}Nb target at two different relative velocities ($V_{rel} \approx 0.053c$, $0.066c$). At $V_{rel} \approx 0.053c$, ^{6}Li ($S_\alpha = 1.47$ MeV), ^{7}Li ($S_\alpha = 2.47$ MeV), and ^{12}C ($S_\alpha = 7.36$ MeV) induced reactions have estimated $F_{ICF} \approx 9.6\%$, 4.6%, and 0.14%, respectively, while at $V_{rel} \approx 0.066c$, the values rise to 13.4%, 5.8%, and 0.25%, respectively. Despite the α-clustered structure possessed by ^{12}C, the larger $S_\alpha = 7.36$ MeV leads to the lower F_{ICF} values compared to others. An increasing F_{ICF} trend with lowering S_α

values is found, marked with an arrow in Fig. 6(a). Higher F_{ICF} values at $V_{rel} \approx 0.066c$ compared to $V_{rel} \approx 0.053c$ for each system demonstrate the projectile energy dependence on ICF. Moreover, the breakup fusion mechanism of ^{12}C is well explained in Ref. [17]. It is worth mentioning that, in all cases, the results are consistent with EMPIRE EGSM level density, thus can be compared to conclude the effect.

Coulomb factor ($Z_P Z_T$). As indicated in several studies [18,19], the Coulomb factor (product of Coulombic charge of the projectile and target) influences the ICF fraction. To project out this effect, F_{ICF} for ^{6}Li + ^{89}Y [26], ^{93}Nb (present data), ^{154}Sm [9] and ^{7}Li + ^{89}Y [30], ^{nat}Zr [49], ^{93}Nb [48], ^{nat}Mo [47] systems are plotted at $V_{rel} \approx 0.066c$ in Fig. 6(b). We observe an increasing trend of F_{ICF} with $Z_P Z_T$ for ^{7}Li induced reactions [Fig. 6(b)] as suggested in Ref. [21], whereas an increasing but different trend for ^{6}Li case is observed in the inset of Fig. 6(b). It is worth noting that the F_{ICF} values for the ^{6}Li + ^{154}Sm system were deduced from the total fusion and ICF cross sections reported in Ref. [9], where the authors used the PACE code; however, the results from rest of the systems are consistent with EMPIRE EGSM level density. Thus, it can be concluded that F_{ICF} is found to increase with $Z_P Z_T$, implying increased ICF observation in reactions with heavy targets (for a particular projectile), in line with well bound α-clustered projectile cases [19,21].

Mass asymmetry (μ). Figure 6(c) depicts F_{ICF} variation as a function of entrance channel mass asymmetry (at $V_{rel} \approx 0.066c$), $\mu = A_T/(A_P + A_T)$, where A_P and A_T are the masses of projectile and target, respectively. Similar increasing trends of F_{ICF} with μ have been observed for ^{6,7}Li reactions as is the case with $Z_P Z_T$. Hence, a larger ICF fraction is concluded in a more asymmetric system in both cases as reflected in published results [18–21] in accordance with Morgenstern's mass asymmetry systematics [51]. However, one may note that the higher F_{ICF} values with mass asymmetry for ^{6}Li reactions over ^{7}Li reactions signify the key role of projectile structure along with the mass asymmetry [20].

Neutron skin thickness (t_N). Imbalance in neutron and proton numbers in heavy nuclei forms a neutron skin on the surface, which is a residual nuclear property. The difference of matter radius (R_m) and charge radius (R_c) i.e., $t_N = R_m - R_c$, defines the neutron skin thickness of a nucleus, calculated as $t_N = \frac{2}{3} r_0 A^{1/3}(I - \delta)$, where $r_0 = 1.16$ fm, $I = \frac{0.4A}{200+A}$; A is the mass number of the target and δ is a density dependent term [52]. Since the ICF process has been considered surface dominant in low energy heavy-ion reactions [53], it would be interesting to project out the effect of neutron skin thickness on the onset of ICF fraction. In this regard, F_{ICF} variation with t_N at $V_{rel} \approx 0.066c$ is reported in Fig. 6(d) for the systems quoted above. An increasing trend of F_{ICF} with t_N was also observed for both ^{6,7}Li cases in consonance with earlier observations [18,20]. However, an extension to even heavier stable targets would fairly confirm the trend observed here (as they exhibit even higher t_N values due to large neutron excess) if F_{ICF} data are available.

Input angular momentum. Entrance channel angular momentum plays a crucial role in the population of CF-ICF channels. In the low energy regime, CF (emerging from the central collisions) is governed by the dominance of short-
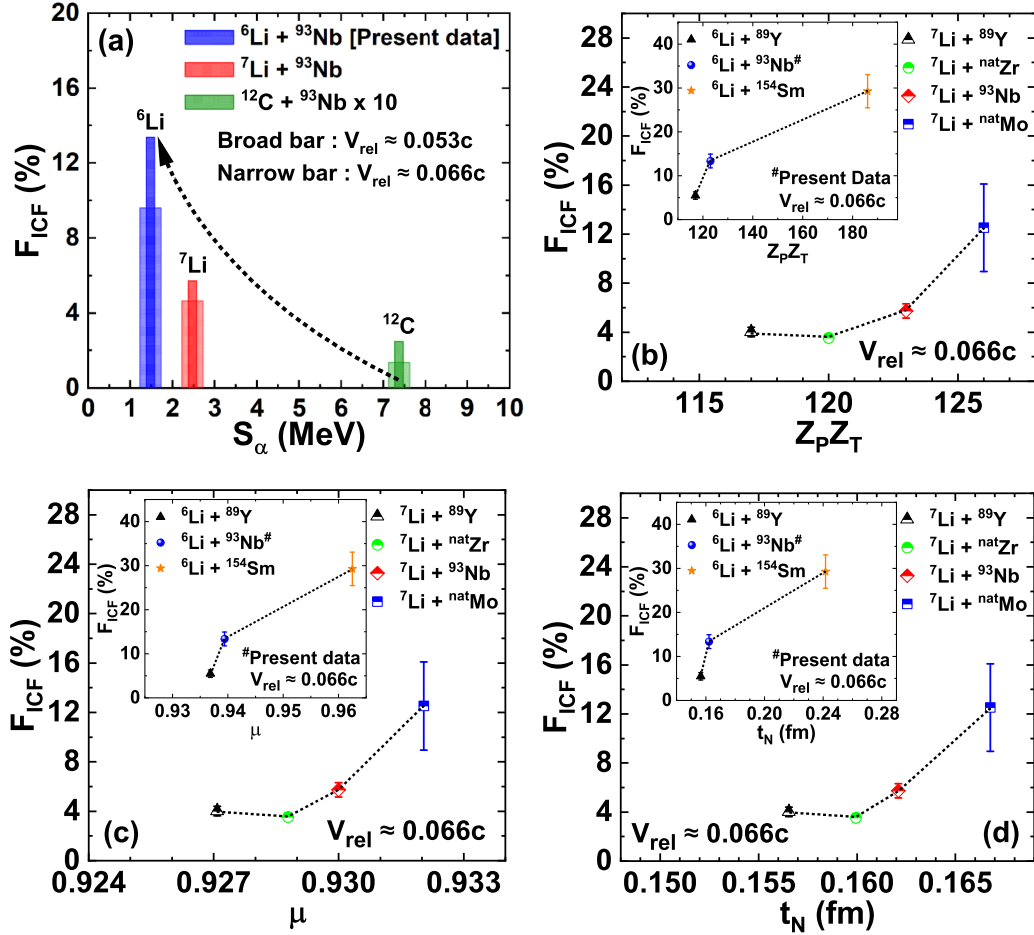
FIG. 6. (a) F_{ICF} systematics with S_α for ^{6}Li, ^{7}Li, ^{12}C reactions on ^{93}Nb at $V_{rel} \approx 0.053c$ (broad bar) and $0.066c$ (narrow bar). The observed trend is marked with an arrow. The values for ^{12}C reaction are multiplied by 10 to make them visible, though the actual values are mentioned in the text. Panels (b), (c), and (d) present the F_{ICF} systematics with $Z_P Z_T$, μ, and t_N, respectively, for ^{7}Li + ^{89}Y, ^{nat}Zr, ^{93}Nb, ^{nat}Mo systems at constant $V_{rel} \approx 0.066c$. Insets of (b), (c), and (d) present the respective systematics for ^{6}Li + ^{89}Y, ^{93}Nb, ^{154}Sm systems at the same $V_{rel} \approx 0.066c$. A line joining the data is to guide the eyes. Refer to the text for details.

range nuclear potential for all the partial waves below a certain limiting value $\ell < \ell_{crit}$ (vanishing limit of the attractive pocket in the entrance channel potential). However, Trautmann *et al.* [53] showed the association of ICF processes with peripheral collisions for $\ell > \ell_{crit}$, whereas, Tricoire *et al.* [54] pointed out the ICF existence for driving angular momentum $\ell < \ell_{crit}$. Wilczyński's formalism [27], based on the sharp cutoff approximation, suggests the population of ICF channels in a localized ℓ space with $\ell \geqslant \ell_{crit}$ and a zero ICF probability below ℓ_{crit}. Employing the original and modified formalisms [27,55], we have simulated the ℓ_{crit} range [26] to understand the role of angular momentum. The maximum angular momentum (ℓ_{max}) corresponding to the peripheral collision was also estimated using $\ell_{max} = R\sqrt{2\mu_m(E_{CM} - V_B)/\hbar^2}$, where R corresponds to the maximum distance between the interacting nuclei such that the collision results in a reaction and V_B is the fusion barrier of the system at a distance R. Table III presents the calculated ℓ_{crit} range and ℓ_{max} values for the systems compared above at $V_{rel} \approx 0.066c$. We infer that, for each system, ℓ_{max} is found to be lesser than the ℓ_{crit} range, implying the contribution of several ℓ bins below

ℓ_{crit} in the population of ICF channels, thus the fusion of ℓ boundaries as observed in previous studies [19,26]. However, the energy dependent critical angular momentum (ℓ_{crit}^{en}) [56], defined as $\ell_{crit}^{en} = C_R[d_0 + d_1\sqrt{(E_{CM} - V_C)}]$, where

TABLE III. Range of critical angular momentum (ℓ_{crit}) [27,55], maximum angular momentum (ℓ_{max}), and energy dependent critical angular momentum (ℓ_{crit}^{en}) [56] values at $V_{rel} \approx 0.066c$ for several systems. In the case of natural targets, values have been calculated for the most abundant isotope.

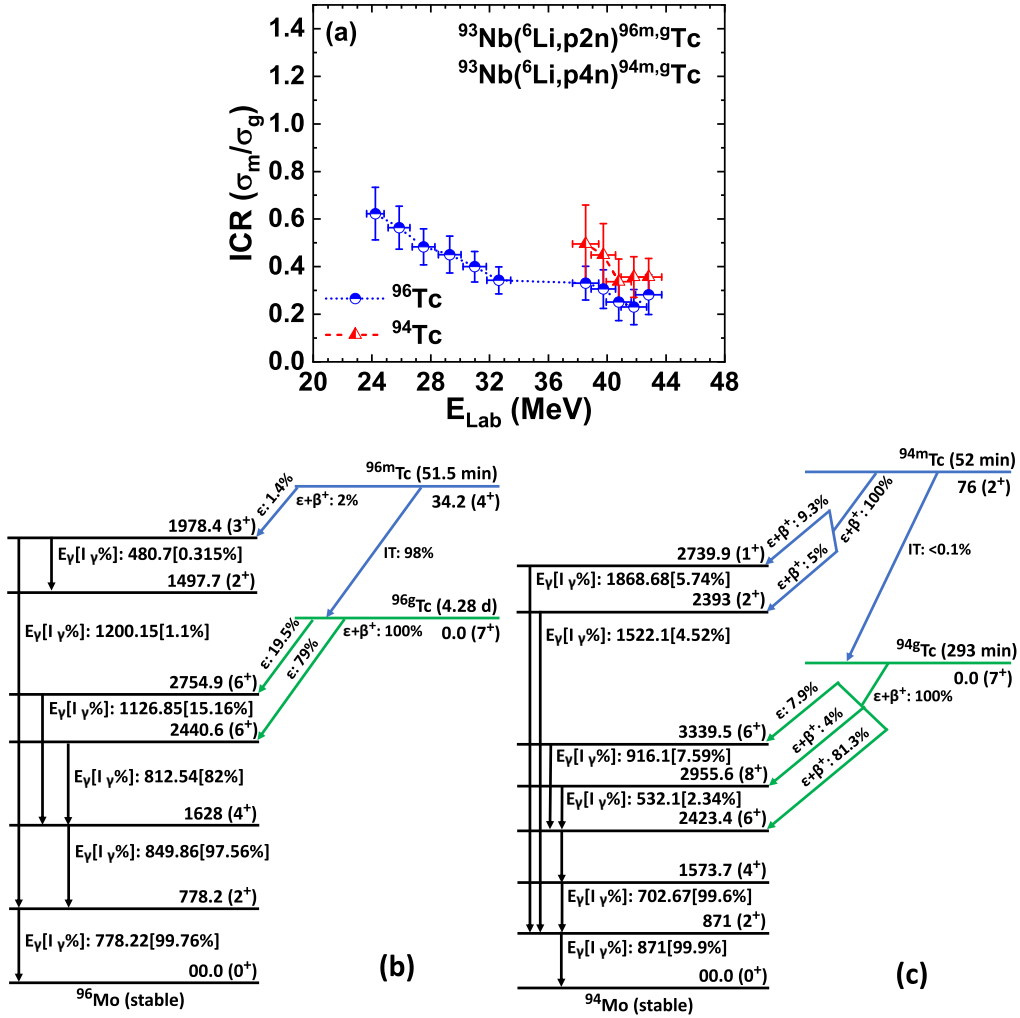| System	ℓ_{crit} range ($\hbar$)	ℓ_{max} ($\hbar$)	ℓ_{crit}^{en} ($\hbar$)
^{6}Li + ^{89}Y	18–25	16	15
^{6}Li + ^{93}Nb	18–26	16	15
^{6}Li + ^{154}Sm	23–31	17	16
^{7}Li + ^{89}Y	21–28	18	17
^{7}Li + ^{90}Zr	21–28	18	17
^{7}Li + ^{93}Nb	21–29	19	17
^{7}Li + ^{98}Mo	22–29	19	18

FIG. 7. (a) Measured isomeric cross section ratio for ^{96,94}Tc radionuclides as a function of projectile energy. Panels (b) and (c) sketch simplified decay schemes of ^{96}Tc and ^{94}Tc radionuclides, respectively, adopted from Ref. [60].

$V_C = 1.18Z_P Z_T/(A_P^{1/3} + A_T^{1/3} + 1.6)$ MeV, $d_0 = 0.33$, $d_1 = 0.205$ MeV^{-1}, and $C_R = \sqrt{A_P A_T/(A_P + A_T)}(A_P^{1/3} + A_T^{1/3})$, lies below $\ell_{\max}$, affirming the obvious ICF occurrence above ℓ_{crit}. Although we have shown the values at $V_{\mathrm{rel}} \approx 0.066c$, the effect was prominent at higher energies for all the systems. Moreover, the $\ell_{\max}$ values computed using CCFULL code [57] (utilizing the Wood-Saxon potential with Akyüz-Winther parametrization varied minimally to reproduce the fusion barrier of the systems) comply with the calculated ones reported in Table III.

D. Isomeric cross section ratio

Relatively long-lived excited states (nuclear isomers) pave the way to understanding nuclear structure, and an isomeric pair populated in a reaction facilitates the determination of isomeric cross section ratio (ICR) [58]. Isomeric cross section ratio (ICR), defined as the ratio of isomeric state to the ground state population, i.e., ICR $= \sigma_m/\sigma_g$, reveals nuclear structure properties such as γ deexcitation and angular mo-

mentum transmutation that take place amid nuclear decays. ICR is altered by the relative spin of isomeric and ground states, projectile energy, and particle emission [49,59]. Figure 7(a) outlines the estimated relative population of the isomeric and ground states of ^{96,94}Tc residues as a function of projectile energy. The measured ICR traces a descending trend with increasing projectile energy up to 32.6 and 40.8 MeV for ^{96}Tc and ^{94}Tc nuclides, respectively, following an almost constant trend above these energies. A remark on the observed trend can be made as follows: ^{96}Tc residue has 7^+ ground state spin and 4^+ isomeric state spin at 0.0 and 34.2 keV, respectively, while ^{94}Tc residue has 7^+ ground state spin and 2^+ isomeric state spin at 0.0 and 76 keV, respectively. A simplified decay scheme of ^{96,94}Tc radionuclides is shown in Figs. 7(b) and 7(c). The CN decay preferably populates the residual high spin states at lower excitation energies, i.e., 7^+ ground state for both the ^{96,94}Tc residues. Enhancing the feeding rate of the ground states with progressive energies rather than metastates in the low energy side resulted in a decrease in ICRs [49] with increasing energy for both cases.

As the energy increases further, the low spin state (metastate) starts populating significantly in both cases. Thus, at higher excitation energies (above 32.6 and 40.8 MeV energies for the respective cases), constancy in the ICR trend is observed, possibly due to an equilibrium between the high and low spin states owing to the large angular momentum release through particle emission from the composite system [49] and/or significant feeding of the metastate through ICF process. Similar trends of ICR have been discussed in earlier reports [49,59].

V. CONCLUSION

The article reports the first excitation function measurement for the ^{6}Li + ^{93}Nb system within the 24–43 MeV energy range. The measured residual excitation functions have been compared with theoretical estimates from the EQ- and PEQ-based statistical model codes like PACE4, EMPIRE3.2.2, and ALICE23 with different level densities to elucidate the underlying reaction dynamics. An exhaustive excitation function analysis revealed the fair reproduction of major xn-channel cross sections by EMPIRE code with EGSM level density, referring to the population of xn-channel residues via the CF mode. However, the manifestation of the PEQ mechanism is evident in the ^{97}Ru residue populated via the $2n$ channel. A substantial enhancement observed in p- and α-emitting channel cross sections accounts for the ICF mechanism in addition to the dominant CF, owing to the low breakup threshold for the ^{6}Li projectile. Thus, the ICF strength fraction of $\approx$8–20% was determined in the studied energy range, obeying an increasing trend with projectile energy. The present result was compared with F_{ICF} deduced for the ^{7}Li reaction on ^{93}Nb to emphasize the projectile structure effect on ICF, and as expected we observed higher F_{ICF} for the ^{6}Li reaction over ^{7}Li, attributed to lower S_α for ^{6}Li. The first ever ICF systematics for weakly bound induced reactions is reported to project the effect of several entrance channel parameters such as bombarding energy, S_α, $Z_P Z_T$, μ, and t_N, and angular momentum on ICF strength fraction for several systems (mentioned in the text) at $V_{rel} \approx 0.066c$. We found an increasing F_{ICF} trend with diminishing S_α. An increasing F_{ICF} trend with rising projectile energy, $Z_P Z_T$, μ, and t_N was concluded for both ^{6,7}Li cases. Though these parameters may play a vital role in ICF dynamics, one cannot quantify their effect on ICF data. Nevertheless, a qualitative assessment of the entrance channel effect can be realized through the present systematics. However, scarcity of ICF data obligates more ICF studies with weakly bound particles extended over the entire mass domain to supplement further the F_{ICF} trend observed in present systematics. Fusion of ℓ boundaries was observed for all the systems compared. The measured ICR trend was also discussed in view of the relative population of isomeric and ground states of ^{96,94}Tc radionuclides.

[1] A. Shrivastava, A. Navin, A. Lemasson, K. Ramachandran, V. Nanal, M. Rejmund, K. Hagino, T. Ichikawa, S. Bhattacharyya, A. Chatterjee *et al.*, Phys. Rev. Lett. **103**, 232702 (2009).

[2] L. F. Canto, P. R. S. Gomes, R. Donangelo, J. Lubian, and M. S. Hussein, Phys. Rep. **596**, 1 (2015).

[3] M. Dasgupta, P. R. S. Gomes, D. J. Hinde, S. B. Moraes, R. M. Anjos, A. C. Berriman, R. D. Butt, N. Carlin, J. Lubian, C. R. Morton *et al.*, Phys. Rev. C **70**, 024606 (2004).

[4] N. T. Zhang, Y. D. Fang, P. R. S. Gomes, J. Lubian, M. L. Liu, X. H. Zhou, G. S. Li, J. G. Wang, S. Guo, Y. H. Qiang *et al.*, Phys. Rev. C **90**, 024621 (2014).

[5] P. K. Rath, S. Santra, N. L. Singh, R. Tripathi, V. V. Parkar, B. K. Nayak, K. Mahata, R. Palit, S. Kumar, S. Mukherjee *et al.*, Phys. Rev. C **79**, 051601(R) (2009).

[6] M. K. Pradhan, A. Mukherjee, P. Basu, A. Goswami, R. Kshetri, S. Roy, P. Roy Chowdhury, M. Saha Sarkar, R. Palit, V. V. Parkar, S. Santra, and M. Ray, Phys. Rev. C **83**, 064606 (2011).

[7] H. Kumawat, V. Jha, V. V. Parkar, B. J. Roy, S. K. Pandit, R. Palit, P. K. Rath, C. S. Palshetkar, S. K. Sharma, S. Thakur *et al.*, Phys. Rev. C **86**, 024607 (2012).

[8] S. P. Hu, G. L. Zhang, J. C. Yang, H. Q. Zhang, P. R. S. Gomes, J. Lubian, X. G. Wu, J. Zhong, C. Y. He, Y. Zheng *et al.*, Phys. Rev. C **91**, 044619 (2015).

[9] C. L. Guo, G. L. Zhang, S. P. Hu, J. C. Yang, H. Q. Zhang, P. R. S. Gomes, J. Lubian, X. G. Wu, J. Zhong, C. Y. He *et al.*, Phys. Rev. C **92**, 014615 (2015).

[10] S. Santra, V. V. Parkar, K. Ramachandran, U. K. Pal, A. Shrivastava, B. J. Roy, B. K. Nayak, A. Chatterjee, R. K. Choudhury, and S. Kailas, Phys. Lett. B **677**, 139 (2009).

[11] D. Chattopadhyay, S. Santra, A. Pal, A. Kundu, K. Ramachandran, R. Tripathi, D. Sarkar, S. Sodaye, B. K. Nayak, A. Saxena *et al.*, Phys. Rev. C **94**, 061602(R) (2016).

[12] D. H. Luong, M. Dasgupta, D. J. Hinde, R. du Rietz, R. Rafiei, C. J. Lin, M. Evers, and A. Diaz-Torres, Phys. Lett. B **695**, 105 (2011).

[13] D. R. Otomar, P. R. S. Gomes, J. Lubian, L. F. Canto, and M. S. Hussein, Phys. Rev. C **87**, 014615 (2013).

[14] M. K. Sharma, M. Kumar, M. Shuaib, V. R. Sharma, A. Yadav, P. P. Singh, B. P. Singh, and R. Prasad, Phys. Rev. C **98**, 054607 (2018).

[15] D. Kumar, M. Maiti, and S. Lahiri, Phys. Rev. C **94**, 044603 (2016).

[16] H. C. Britt and A. R. Quinton, Phys. Rev. **124**, 877 (1961).

[17] M. Sagwal, M. Maiti, T. N. Nag, and S. Sodaye, Eur. Phys. J. Plus **136**, 1057 (2021).

[18] A. Agarwal, A. K. Jashwal, M. Kumar, S. Prajapati, S. Dutt, M. Gull, I. A. Rizvi, K. Kumar, S. Ali, A. Yadav *et al.*, Phys. Rev. C **103**, 034602 (2021).

[19] M. Shuaib, V. R. Sharma, A. Yadav, M. K. Sharma, P. P. Singh, D. P. Singh, R. Kumar, R. P. Singh, S. Muralithar, and B. P. Singh, J. Phys. G: Nucl. Part. Phys. **44**, 105108 (2017).

[20] R. N. Sahoo, M. Kaushik, A. Sood, P. Kumar, V. R. Sharma, A. Yadav, P. P. Singh, M. K. Sharma, R. Kumar, B. P. Singh *et al.*, Nucl. Phys. A **983**, 145 (2019).

[21] P. K. Giri, D. Singh, A. Mahato, S. B. Linda, H. Kumar, S. A. Tali, S. Parasari, A. Ali, M. A. Ansari, R. Dubey *et al.*, Phys. Rev. C **100**, 024621 (2019).

[22] M. Gull, K. Kumar, S. Ali, T. Ahmad, S. Dutt, I. A. Rizvi, A. Agarwal, and R. Kumar, Phys. Rev. C **98**, 034603 (2018).

[23] M. Maiti, Phys. Rev. C **84**, 044615 (2011).

[24] M. Maiti and S. Lahiri, Phys. Rev. C **84**, 067601 (2011).

[25] R. Rafiei, R. du Rietz, D. H. Luong, D. J. Hinde, M. Dasgupta, M. Evers, and A. Diaz-Torres, Phys. Rev. C **81**, 024601 (2010).

[26] R. Prajapat and M. Maiti, Phys. Rev. C **103**, 034620 (2021).

[27] J. Wilczyński, Nucl. Phys. A **216**, 386 (1973).

[28] J. F. Ziegler, M. D. Ziegler, and J. P. Biersack, Nucl. Instrum. Methods Phys. Res. Sect. B **268**, 1818 (2010).

[29] A. Singh, M. Maiti, T. N. Nag, and S. Sodaye, Phys. Scr. **98**, 025306 (2023).

[30] R. Prajapat and M. Maiti, Phys. Rev. C **101**, 024608 (2020).

[31] National Nuclear Data Center, Brookhaven National Laboratory, https://www.nndc.bnl.gov/nudat3/.

[32] A. Gavron, Phys. Rev. C **21**, 230 (1980).

[33] M. Herman, R. Capote, B. V. Carlson, P. Oblozinsky, M. Sin, A. Trkov, H. Wienke, and V. Zerkin, Nucl. Data Sheets **108**, 2655 (2007).

[34] M. Blann, Phys. Rev. C **54**, 1341 (1996).

[35] W. Hauser and H. Feshbach, Phys. Rev. **87**, 366 (1952).

[36] C. M. Perey and F. G. Perey, At. Data Nucl. Data Tables **17**, 1 (1976).

[37] A. J. Koning and J. P. Delaroche, Nucl. Phys. A **713**, 231 (2003).

[38] H. An and C. Cai, Phys. Rev. C **73**, 054605 (2006).

[39] F. D. Becchetti and G. W. Greenlees, Phys. Rev. **182**, 1190 (1969).

[40] V. Avrigeanu, P. E. Hodgson, and M. Avrigeanu, Phys. Rev. C **49**, 2136 (1994).

[41] R. Capote, M. Herman, P. Obložinský, P. G. Young, S. Goriely, T. Belgya, A. V. Ignatyuk, A. J. Koning, S. Hilaire, V. A. Plujko *et al.*, Nucl. Data Sheets **110**, 3107 (2009).

[42] A. D'Arrigo, G. Giardina, M. Herman, A. V. Ignatyuk, and A. Taccone, J. Phys. G: Nucl. Part. Phys. **20**, 365 (1994).

[43] A. V. Ignatyuk, J. L. Weil, S. Raman, and S. Kahane, Phys. Rev. C **47**, 1504 (1993).

[44] A. Gilbert and A. G. W. Cameron, Can. J. Phys. **43**, 1446 (1965).

[45] V. F. Weisskopf and D. H. Ewing, Phys. Rev. **57**, 472 (1940).

[46] R. Kumar, M. Maiti, T. N. Nag, and S. Sodaye, Phys. Rev. C **104**, 064606 (2021).

[47] D. Kumar, M. Maiti, and S. Lahiri, Phys. Rev. C **96**, 014617 (2017).

[48] D. Kumar and M. Maiti, Phys. Rev. C **96**, 044624 (2017).

[49] R. Prajapat and M. Maiti, Phys. Rev. C **101**, 064620 (2020).

[50] S. Santra, S. Kailas, V. V. Parkar, K. Ramachandran, V. Jha, A. Chatterjee, P. K. Rath, and A. Parihari, Phys. Rev. C **85**, 014612 (2012).

[51] H. Morgenstern, W. Bohne, W. Galster, K. Grabisch, and A. Kyanowski, Phys. Rev. Lett. **52**, 1104 (1984).

[52] W. D. Myers, Phys. Lett. B **30**, 451 (1969).

[53] W. Trautmann, O. Hansen, H. Tricoire, W. Hering, R. Ritzka, and W. Trombik, Phys. Rev. Lett. **53**, 1630 (1984).

[54] H. Tricoire, C. Gerschel, N. Perrin, H. Sergolle, L. Valentin, D. Bachelie, H. Doubre, and J. Gizon, Z. Phys. A **306**, 127 (1982).

[55] J. Wilczyński, K. Siwek-Wilczyńska, J. van Driel, S. Gonggrijp, D. C. J. M. Hageman, R. V. F. Janssens, J. Łukasiak, and R. H. Siemssen, Phys. Rev. Lett. **45**, 606 (1980).

[56] M. V. Chushnyakova and I. I. Gontchar, Nucl. Phys. A **941**, 255 (2015).

[57] K. Hagino, N. Rowley, and A. T. Kruppa, Comput. Phys. Commun. **123**, 143 (1999).

[58] P. Walker and Z. Podolyák, Phys. Scr. **95**, 044004 (2020).

[59] R. Kumar, R. Prajapat, and M. Maiti, J. Phys. G: Nucl. Part. Phys. **50**, 025106 (2023).

[60] D. Abriola and A. A. Sonzogni, Nucl. Data Sheets **109**, 2501 (2008); **107**, 2423 (2006).